Complex aero-engine intake ducts and dynamic distortion

David G. MacManus[1], Nicola Chiereghin[2], Daniel Gil Prieto[3] and Pavlos Zachos[4]
Cranfield University, Bedfordshire, MK43 0AL, United Kingdom

For many embedded and partially-embedded engine systems, the complexity of the flow field associated with convoluted intakes presents an area of notable research challenges. The convolution of the intake duct introduces additional flow distortion and unsteadiness which must be understood and quantified when designing the turbomachinery components. The aim of the current work is to investigate the capabilities of modern computational methods for these types of complex flows, to study the unsteady characteristics of the flow field and to explore the use of proper orthogonal decomposition methods to understand the nature of the unsteady flow distortion. The unsteady flow field for a range of S-duct configurations has been simulated and assessed using a delayed detached eddy simulation method. The configurations encompass the effects of Mach number, Reynolds number and S-duct centreline offset distance. Analysis of the conventional distortion criteria highlights the main sensitivities to the S-duct configuration and quantifies the unsteady range of these parameters. These results illustrate the strongly dynamic nature of the flow field for both total pressure as well as swirl based distortion. Analysis of the unsteady flow field shows signature regions of unsteadiness which are postulated to be related to the classical secondary flows as well as to the streamwise flow separation. The more aggressive duct, with a larger centreline offset, shows some similar characteristics, but the unsteadiness is more broadband and the distinction between these two mechanisms is less clear. A proper orthogonal decomposition of the total pressure field at the duct exit identifies the underpinning flow modes which are associated with the overall total pressure unsteadiness distributions. For the more aggressive duct, the flow modes are notably different and highlight the reduced demarcation between the unsteady flow field mechanisms.

Nomenclature

p	=	static pressure
p_o	=	total pressure
r	=	cross section radius
max	=	maximum value of a temporal distribution
min	=	minimum value of a temporal distribution
s	=	S-duct curvilinear coordinate along the axis
t_c	=	convective time = L_s/w_{in}
u, v, w	=	velocity vector components
v_θ	=	tangential velocity
x, y, z	=	system of reference coordinates
D	=	diameter
L_s	=	S-Duct length measured along the centreline
Ma	=	Mach number
R	=	S-duct curvature radius
Re	=	diameter-based Reynolds number
α	=	swirl angle

---

[1] Senior Lecturer, Propulsion Engineering Centre, Building 52, Cranfield University, AIAA Member.
[2] PhD Student, Propulsion Engineering Centre, Building 52, Cranfield University.
[3] PhD Student, Propulsion Engineering Centre, Building 52, Cranfield University.
[4] Lecturer, Propulsion Engineering Centre, Building 52, Cranfield University, AIAA Member.

1

Δt	=	unsteady simulation time step
Δt^*	=	non-dimensional time step = $\Delta t/t_c$
Δz_{out}	=	distance downstream the S-Duct outlet along the z-axis
Θ	=	angular position on the AIP
Φ	=	S-duct angular position

Subscripts

AIP	=	aerodynamic interface plane
Avg	=	area-average
in	=	inlet
Θ	=	tangential direction
$<p0>$	=	referred to the time-averaged distribution of p0
$<\alpha>$	=	referred to the time-averaged distribution of α

Operators

$(\cdot)$	=	time-average
$\overline{}$	=	area-average
$\sigma.$	=	standard deviation
i	=	ring index where i=0 refers to the inner ring

I. Introduction

Future aircraft engine configurations are expected to require a closer coupling between the propulsion system and the airframe, with potential benefits in term of drag, noise and reduction in observability. For many embedded and partially-embedded engine systems, the complexity of the flow field associated with convoluted intakes presents an area of notable research challenges. The development of embedded engine configurations leads to the intake and duct aerodynamics having greater importance since they play a vital role in engine operability and performance[1]. The convolution of the intake duct introduces additional flow distortion and unsteadiness which must be understood and quantified when designing the turbomachinery components. Current industry practice for characterising distorted flow fields into compressor or fan systems is known to have limitations for predicting instability onset[1]. Consequently the risk may be carried forward into full scale testing. This can sometimes lead to late design changes as happened for example during the development of Tornado, a twin-engine fighter equipped with a pair of side-mounted intakes with horizontal S-Ducts. The compatibility was initially tested by total pressure measurements, which found total pressure distortion within allowable limits. However, initial flight tests found several intake-engine compatibility problems, like surge of the port engine at subsonic speed with high angle of attack and starboard surge at supersonic speed[2].

Complex intake aerodynamic distortion is usually characterized by total pressure, temperature and swirl non uniformities. A loss of performance in term of surge margin is observed when the distorted area extends circumferentially beyond a critical angle[1] which depends on the compressor characteristics. Several metrics have been proposed to quantify total pressure distortion from measurements[3]. Swirl can be related to vortices and secondary flow and modifies the nominal incidence angle of the flow to the blade with the risk of unexpected stall. A further degradation of engine performance was observed when total pressure distortion is combined with a bulk swirl counter-rotating with respect to the compressor rotation direction[2]. This was also evident in the experimental investigation of wing tip vortex ingestion by Mitchell[4], with the greatest loss observed when a counter-rotating vortex was located close to the compressor hub. In such an event, the stall arose at a pressure ratio closer to the normal operating line in comparison with the undistorted condition[5]. The effect of a twin swirl pattern was experimentally observed in Mayer et al[6], where twin vortices where generated by means of a delta wing with variable angle of attack. The intensity of the vortices was quantified as the area average swirl angle and an increase in average swirl angle was observed to produce an increase in loss of surge margin, despite a modest value of 0.15 of the total pressure distortion coefficient DC(60). A reduction of 26% of the surge margin was observed with an average swirl angle of 13 degrees, together with a reduction of 7% of the compressor efficiency.

Initially distortion was typically quantified from the time-averaged distribution of total pressure and velocity. However, previous studies noted that engine stall can be generated from distortion fluctuations [7] and highlighted the importance of the turbulence levels. Further studies of dynamic distortion emphasized the importance of instantaneous distortion and in particular the local peak values. For example, for an engine operating under steady

operating conditions a stall was observed after several minutes, which indicates an association with a rare distortion characteristic[7]. Within this context, the aim of the current work is to investigate the capabilities of modern computational methods for these types of complex flows, to study the unsteady characteristics of the flow field and to explore the use of proper orthogonal decomposition methods to understand the nature of the unsteady flow distortion.

A number of previous studies have assessed the flow distortion associated with S-duct configurations. Wellborn et al[8] undertook an experimental study of the flow through a diffusing S-duct. The total pressure distribution at the AIP showed a low-pressure zone on the lower part. Wall static pressure measurements and flow visualization demonstrated that this effect is associated with a large separation generated in the first part of the duct. The flow field also featured strong secondary flows which led to the generation of a pair of contra-rotating vortices at the AIP. This test case has been used to evaluate computational methods and a comparison between different turbulence models for steady RANS simulations was performed by Delot et al[9] and Fiola et al[10]. These results show a reasonable capability of well-established turbulence models, like Spalart-Allmaras and k-ω SST, to represent the behaviour of highly separated flow typical of a highly convoluted intake. Although the models could not accurately predict simultaneously all the performance parameters such as pressure recovery and total pressure distortion, it demonstrated the capability of k-ω SST to broadly capture the flow physics. However, high bandwidth pressure measurements in two S-duct configurations with different centreline offsets[11,12] demonstrated notable unsteadiness in the separation region which produces oscillations of the flow distortions at the exit plane. The measurement of the total pressure standard deviation at the AIP reported in Delot et al[11] outlined fluctuations up to 3.5% of the inlet total pressure with an AIP Mach number of about 0.4. Spectral and cross-correlation analysis of the signal suggested that the fluctuations are mainly associated with a horizontal and a vertical oscillation of the total pressure distribution.

The recent improvement in computational resources and computational fluid dynamics (CFD) presents an opportunity to simulate also the dynamic behaviour of flow distortion in such complex intake geometries. An additional aspect with modern CFD methods is offered by scale-resolving transient simulations, which can improve the performance of unsteady Reynolds Averaged Navier-Stokes methods and provide the possibility to simulate the time-variant issues of unsteady flow distortion. Large Eddy Simulations directly resolve the turbulent structures which are larger than the numerical grid and use a universal model to simulate the effect of sub-grid scale, which are assumed to be isotropic and independent from the boundary conditions. The grid size must be sufficiently fine to make this hypothesis realistic. Nevertheless this still demands substantial computational resources. Coherent non-isotropic structures are observed also for very small scales, in the order of Kolmogorov scales, close to the wall in flows with high Reynolds numbers typical of aeronautical applications and would require a mesh resolution similar to DNS. A useful compromise is offered by Detached-Eddy simulations (DES) where the RANS equations are applied close to the wall, while the rest of the flow is solved by LES equations and present an opportunity to simulate the dynamic behaviour of flow distortion in such complex intake geometries.

Berens et al[13] and Delot[14] demonstrated the capability of DES to reproduce the strongly turbulent behaviour of the flow observed in curved intakes which was in notable contrast with unsteady RANS simulations which provided a non-realistic almost stationary solution. Both studies compared RANS and URANS simulations with Zonal-DES and DES combined with Spalart-Allmaras and algebraic Reynolds stress turbulence models. These studies demonstrated the capability of DES to capture the highly unsteady nature of flow separations in S-Ducts[13] and serpentine ducts[14] with remarkable oscillations observed for DC(60), RDI and CDI with peak values almost double the average value. Furthermore, URANS calculations did not reproduce the flow instabilities typical of S-duct separations and resulted in a unrealistically predominately steady flow.

This current research extends the work on flow distortion simulation with a study of the effect of duct geometry (offset), Reynolds number and Mach number. The capability of DES to predict the change in performance for different configurations is assessed through a comparison with experimental data[11, 12]. For a better understanding of the dynamic distortion issues, a Proper Orthogonal Decomposition (POD) of the total pressure variations at the S-duct exit plane is also performed. The POD analysis is used to evaluate the impact of specific modes on the distortion statistics and to identify the total pressure modes that have the most notable impact on the dynamic distortion.

II. S-duct configurations

In this research, the S-duct configurations previously experimentally investigated by Wellborn[8], Garnier[12] and Delot[11] were considered. A schematic representation is provided in Fig. 1. The centerline is composed of two opposite circular arcs with an extension of $\varphi_{max}/2$ with the nominal aerodynamic interface plane (AIP) at the duct

exit. A diffusion area ratio of 1.52 was fixed for all the configurations (Table 1). In this work, three different geometric configurations were considered with the main parameters defined in Table 1. S-Duct 1 has the same dimensions of the geometry experimentally investigated by Wellborn et al[8]. S-Duct 2 maintains the same non-dimensional offset H_0/L and length L/D_{in} as in S-Duct 1 but with a reduced inlet diameter and concomitant reduction in Reynolds number (Table 2). S-Duct 3 is related to S-Duct 2 but with an increase of the offset H_0/L from 0.268 to 0.493. These configurations were used to perform a range of simulations with nominal flow conditions outlined in Table 2 where Ma_{cl} indicates the value of centreline Mach number $0.5D_{in}$ upstream of the start of the S-Duct section. The comparison between S-Duct 1 and S-Duct 2A provides an assessment of the effect of the scaling on the S-Duct performance. An assessment of the influence of Mach number is obtained from S-Duct 2A and 2B as well as Duct-3A and -3B. Finally, the assessment of the effect of the offset (H_0/L) is obtained from the comparison between S-Duct 2 and 3. These assessments are performed on a cross-sectional plane at a distance Δz_{out} of $0.5D_{in}$ downstream the S-Duct outlet (section AIP in Fig. 1). For a validation, a separate simulation has been performed with the geometry in Fig. 2, which includes a spinner downstream of the S-Duct and is more representative of the experimental condition in Delot et al [9,11]. The geometrical characteristics of this S-Duct (Duct 2BS) are the same as S-Duct 2B in Table 1. The comparison between numerical and experimental results is performed at the AIP2 section (Fig. 2), at Δz_{out} of $0.36D_{in}$, where steady and transient total pressure measurements with a 40 Kulite rake were taken in Delot et al[11]. The experimental model was manufactured and tested at the ONERA wind tunnel R4MA (Modane-Avrieux, France) in 2006 and 2008. The geometry is based on a smaller scale model developed by Harloff et al. at NASA Lewis Research Center in the 1990's[15].
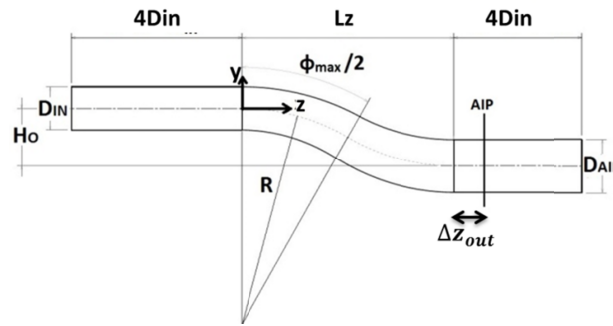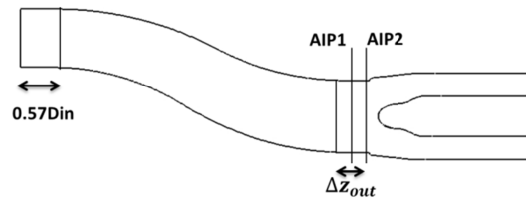

Figure 1 Schematic of S-duct geometry

Figure 2 Geometrical representation of the S-Duct 2BS from Delot et al.[10]

4

Table 1 S-duct geometry parameters

Parameters	S-Duct 1	S-Duct 2	S-Duct 3
A_{out}/A_{in}	1.52	1.52	1.52
L/D_{in}	5.0	5.0	4.95
H_o/L	0.268	0.268	0.493
ϕ_{max} [°]	60	60	105.1
D_{in} [m]	0.2042	0.133	0.133
D_{out} [m]	0.2514	0.164	0.164
R [m]	1.021	0.665	0.4146
L [m]	1.021	0.665	0.658
H_o [m]	0.2736	0.1784	0.3245

Table 2 : Test cases and flow conditions

Case	AIP Ma	Ma_{CL}	Inlet Re_{Din}	Δt
S-duct 1	0.36	0.6	2.6×10^6	6.0×10^{-6} s
S-duct 2A	0.36	0.6	1.7×10^6	6.0×10^{-6} s
S-duct 2B	0.18	0.28	1.1×10^6	12×10^{-6} s
S-Duct 2BS	0.18	0.28	1.1×10^6	12×10^{-6} s
S-duct 3A	0.39	0.65	1.8×10^6	6.0×10^{-6} s
S-Duct 3B	0.18	0.28	1.1×10^6	12×10^{-6} s

III. Methodology

A. CFD method

The calculations are performed using a Delayed Detached-Eddy-Simulation (DES) where the flow field is calculated with RANS equations close to the wall, whilst the highly-unsteady zones, in particular after the separation, are calculated with LES[14]. The Delayed version of the DES (DDES) is used to prevent grid-induced separation problems as reported in previous versions of DES[16,17]. In this current work the k-ω SST turbulence model was chosen for the closure of the RANS equations. A pressure-based solver was selected with a segregated PISO scheme[18,19]. A second-order spatial interpolation scheme was used for the pressure equations and the third order MUSCL scheme for momentum, energy and turbulence. An iterative time advancement scheme with a bounded second-order temporal discretization method was used[18,19]. The inlet boundary condition comprised specified uniform total pressure and total temperature profile. The static pressure was specified at the domain exit and was adjusted to provide the required average Mach number at the AIP. The inlet domain extent of $4D_{in}$ resulted in the growth of the duct boundary layer. For S-Duct 1, Wellborn reported a measured inlet boundary layer thickness at a location of Z/D_i of –0.5 upstream of the S-Duct inlet plane. At an AIP Mach number of 0.36, the measured boundary layer had a compressible displacement thickness of $1.46r_{in}$ and a shape factor of 1.38. The time average computed boundary layer for the medium mesh had a boundary layer displacement thickness of $1.76r_{in}$ and shape factor of 1.39.

B. Computational grid

A baseline structured mesh with a size of 5.9 million of nodes was created using a multi-blocking strategy. To maintain the mesh orthogonality to the wall for every configuration, four different blocks were created: the first associated with the inlet straight duct, the second and the third with the S-Duct, and the forth with the straight duct downstream the S-Duct. The mesh has an H-grid structure in the central part of the duct, and an O-grid structure around the wall. The robustness of the method and the simplicity of the geometry allowed a good quality of the mesh for every case, with a 2x2x2 determinant greater than 0.8. The mesh was clustered towards the wall to ensure that y^+ was less than 1 over the full domain.

An initial grid sensitivity study has been carried out for the S-duct 2A and three RANS calculations using the k-ω SST turbulence model were performed with spatial resolution of 3.1, 5.9 and 11.2 million nodes for the coarse, medium and fine meshes, respectively. The sensitivity of the mesh dependence was considered in terms of the total pressure ratio (PR) between the inlet and the AIP and the total pressure distortion based on the CDI metric. Between the medium and fine mesh the PR increased by 0.07% and CDI reduced by 0.7%. The grid convergence index for CDI was 0.12% and using the Richardson extrapolation[20] the discretization error was estimated at 0.8% for CDI.

The effect of the mesh resolution on the unsteady aerodynamics was evaluated for S-duct 2A with a nominal AIP Mach number of 0.36 (Table 2). Unsteady calculations were performed using the same meshes as for the RANS mesh sensitivity study. An unsteady analysis using the medium mesh was performed with a time step Δt of 6×10^{-6} s. In order to maintain a similar Courant number, a time step of 5×10^{-6} s was used for the fine mesh, and 10×10^{-6} s for the coarse mesh. The data was analysed for 55 convective time scales after the initial transient from the steady RANS solution. The convective time t_c is defined in terms of the S-Duct curvilinear length and time-averaged inlet velocity. The impact of the mesh resolution on the time averaged PR showed a variation of time-averaged PR of 0.05% from the medium to fine mesh. The distortion metrics are more sensitive to the spatial resolution and are not conserved thermodynamic properties. A monotonic variation was observed for the time-averaged total pressure distortion parameters DC60, RDI, CDI. Between the medium and fine mesh simulations the time averaged RDI decreased by 1.8% and CDI and DC60 increased by 4.6 and 8.0%, respectively. Non-monotonic variation was observed for the time averaged swirl intensity ($\overline{SI}$) in the comparison of the three grid sizes, with an increase of 3.2% from the medium to fine mesh.

The impact of the mesh refinement on the unsteady aspects was also evaluated for the unsteady data of 55 mean convective time periods. The standard deviation of PR changed monotonically as the mesh size increased and there was a 5.7% decrease between the medium and fine meshes. The sensitivity of the distortion metrics was greater. Between the medium and fine mesh, a variation of up to 13% was observed for the standard deviation of the total pressure distortion parameters DC(60), RDI and CDI, while the standard deviation of swirl intensity (SI) increased by 2.1%. The results presented in this paper were performed using a medium mesh for all configurations.

C. Computational time steps

A time step Δt of 6×10^{-6} s was chosen for the high Mach number cases (S-Duct 1, 2A, 3A) and 1.2×10^{-5} s for the low Mach cases (S-Duct 2B, 2BS, 3B) which correspond to a non-dimensional time step Δt of approximately 0.002 with respect to the mean overall convective time through the duct. To assess the impact of the time step, the S-Duct 2A case was also simulated with a time step of 12×10^{-6} s and the time average and unsteady distortion metrics were compared. With regard to the time averaged values, pressure recovery and RDI decreased by less than 0.1% with time step reduction from 12 to 6×10^{-6} s. Time-averaged swirl intensity $\overline{(SI)}$ decreased by 0.2% while CDI and DC60 increased by 3%. The unsteady characteristics were more sensitive to the change in time step with variations of standard deviation of CDI, RDI, DC60 and SI of up 7% with this time step reduction. A variation of 2% was observed for the standard deviation of pressure recovery.

The DDES calculations were initialized from converged RANS simulations with residuals of an order of magnitude of 10^{-7}. Each time step was calculated using 20 sub iterations which typically resulted in residuals in the order of 10^{-6} for continuity equation and 10^{-7} for momentum, energy, k and ω equations, with a reduction of at least three orders of magnitude of all the residuals from start to end of the time step sub iterations. For all the cases, an interval of 15 convective times where used as a transition between the steady solution and the established unsteady flow field. Data from this initial transient were discarded and not included in the analysis of the final results. To assess the sensitivity of the results to the length of the simulated time interval the time-averaged and standard deviation of the key parameters was evaluated for simulated periods ranging from 15 to about 65 convective times. It was observed that between 50 and 65 convective times the averaged PR across these range of simulation periods varied by less than 0.1% and the standard deviation of PR changed by 2.5%. Similarly for the distortion metrics, the time-averaged DC60, CDI, RDI and SI all changed by less than 1% and the standard deviation varied by less than 2.5% between 50 and 65 convective times. A simulation length of 55 convective times was used for the statistical and spectral analysis as well as for the POD assessment.

D. Distortion metrics

This paper focuses on both total pressure and swirl distortion. The importance of the effect of flow non-uniformities on an aero-engine has resulted in the development of a range of reduced order parameters to quantify the level of distortion being presented to the engine[2]. Most of this previous work has focused on total pressure and total temperature distortion although the possible importance of swirl distortion is also acknowledged[2]. In particular, the more detrimental effects on the engine performance were observed when total pressure distortion is combined

with swirling vortical structures[2]. To perform a quantitative assessment of distortion, several parameters have been proposed based on measurements of total pressure, axial and tangential velocity[3]. Such measurements are typically distributed on equal area rings which gives a distributed radial spacing of the probes (Fig. 3). For every ring a number of equi-spaced measurement points are circumferentially distributed (typically 8). Most of the experimental data currently available refers to such measurement distribution. For the computational work the spatial resolution at the AIP is several orders of magnitude greater than that of an 8x5 rake. The aerodynamic parameters are linearly interpolated from the computational mesh onto the 8x5 locii. The area-average total pressure of the AIP, ($\overline{p0_{AIP}}$), is calculated as the mean value of these 40 points.

Ring index i	r/r_{AIP}
0	0.3162
1	0.5477
2	0.7071
3	0.8367
4	0.9487
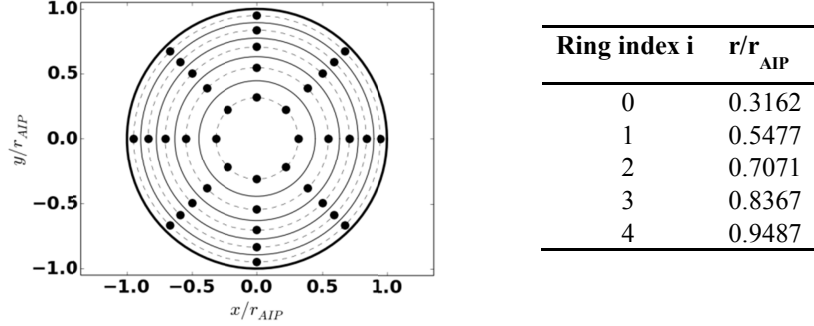
Figure 3 Standard rake for flow distortion descriptors calculation[21].

One of the main industry standards has been developed by the Society of Automotive Engineering (SAE) which proposes a variety of conventional distortion descriptors which are used to evaluate the levels of distortion. Many of these parameters relate to total pressure distortion at the AIP and include sectional distortion coefficient DC(60), circumferential distortion index (CDI) and radial distortion index (RDI). DC(60) is defined by the difference between the average total pressure ($\overline{p0_{AIP}}$) and the lowest average total pressure in a sector of 60° angle ($\overline{p0_{60}}$) and is non-dimensionalized by the mean dynamic head of the whole AIP (Eq. 1):

$$DC(60) = \frac{\overline{p0_{AIP}} - \overline{p0_{60}}}{\bar{q}} \tag{1}$$

It is acknowledged that the effect of circumferential non-uniformities on the aero-engine compression system is likely to be different due to the impact of the radial non-uniformities. The circumferential distortion index (CDI) assesses the uniformity of the circumferential total pressure distribution at a specific radial position and is defined in Eq. 2[3]:

$$CDI = Max_{i=0}^{4}\left(0.5\left[\frac{\overline{p0}_i - min(p0)_i}{\overline{p0_{AIP}}} + \frac{\overline{p0}_{i+1} - min(p0)_{i+1}}{\overline{p0_{AIP}}}\right]\right) \tag{2}$$

where $\overline{p0_{AIP}}$ is the average total pressure at the AIP, $\overline{p0}_i$ is the average total pressure of the circumferential pressure distribution of the i-th ring and $min(p0)_i$ is the minimum pressure along this same ring. Non-uniformities in the radial distortion were evaluated by the radial distortion index (RDI) which broadly follows the same construct as CDI and is defined in Eq. 3:

$$RDI = Max\left(\frac{\overline{p0_{AIP}} - \overline{p0}_{i=0}}{\overline{p0_{AIP}}}, \frac{\overline{p0_{AIP}} - \overline{p0}_{i=4}}{\overline{p0_{AIP}}}\right) \tag{3}$$

with $\overline{p0}_{i=0}$ the average total pressure of the pressure distribution of the inner ring and $\overline{p0}_{i=4}$ is the average total pressure at the outer ring.

The distortion descriptors for swirl based non-uniformities are not as well established as the parameters based around total pressure distortion. Nevertheless, swirl distortion can be considered in terms of an SC(60)[21] and a swirl intensity parameter[2]. SC(60) is broadly analogous to the total pressure DC(60) although the validation of the

parameter is not as well established. SC(60) is defined as the ratio of $max(|\overline{V_{\theta\,60}}|)$, the maximum average circumferential velocity in a section of 60°, to the mean axial velocity $\overline{w_{AIP}}$ as defined in Eq. 4[22]:

$$SC(60) = \frac{max(|\overline{V_{\theta\,60}}|)}{\overline{w_{AIP}}} \tag{4}$$

The swirl angle α is defined as the circumferential angle between the velocity vector and the axial velocity vector. The Society of Automotive Engineering (SAE) defined total pressure distortion as a ring-based radial distribution of specific parameters where radial and circumferential distortions are quantified separately. The circumferential distortion is defined in term of extent, intensity and multiple-per-revolution. The circumferential total pressure distribution p0 is considered in terms of an average $\overline{p0}_i$ and regions of low relative total pressure (p0< $\overline{p0}_i$) and high relative total pressure (p0> $\overline{p0}_i$). The extent element, θ_i^-, is defined as the circumferential extension of the low pressure region[21]. If only a single low pressure region is obtained for an individual circumferential ring i, the extent parameter is calculated as follows (Fig. 4):

$$\theta_i^- = \theta2_i - \theta1_i \tag{5}$$

The extent parameter provides an indication of the time spent in the low pressure zone by a compressor blade during a revolution period. Significant effects on performance are observed only for θ_i^- higher than a critical angle depending on the compressor time constant and rotation speed. Cousins[1, 23] suggests to calculate the time constant of axial compressors as the time for a particle to travel from the airfoil leading edge to the throat of the blade passage where the diffusion process starts. Another aspect of the circumferential distortion to be considered is its amplitude, which is quantified by the circumferential distortion intensity for the ring i is defined as:

$$(\Delta P_C/P)_i = \left(\frac{\overline{p0}_i - \overline{p0_-}}{\overline{p0}_i}\right)_i \tag{6}$$

where:

$$(\overline{p0_-})_i = \frac{1}{\theta_i^-}\int_{\theta1_i}^{\theta2_i} p0(\theta)_i d\theta \tag{7}$$

is the average value of the total pressure in the low pressure region. Therefore, this element provides a numerical indication of the magnitude of the load added to a blade by total pressure distortion. This can be related to mechanical aspects, in terms of amplitude of the blade vibration, and aerodynamic effects in terms of higher work necessary to deliver the same outlet pressure as for the undistorted part. In the case of multiple pressure regions, a circumferential distortion intensity $(\Delta P_C/P)_{i,k}$ and extent $\theta_{i,k}^-$ are calculated for every low pressure region k, and the extent and circumferential intensity value assigned to the ring i is the one corresponding to the low pressure region with the biggest area, that is[21]:

$$(\Delta P_C/P)_i = (\Delta P_C/P)_{i,kmax} \tag{8}$$

$$\theta_i^- = \theta_{i,kmax}^- \tag{9}$$

where:

$$(kmax)_i = \left(argmax_{k=1,..,Q}\ (\Delta P_C/P)_{i,k}\ \theta_{i,k}^-\right)_i \tag{10}$$

and Q is the number of low pressure region. The circumferential extension of this region is the value assigned to the extent element θ_i^- of the ring. A pattern of two or more adjacent low pressure regions separated by high pressure regions with extension smaller than a reference circumferential extension θ_{min}^+ is considered as a single equivalent low pressure region. In this work taken as 25°. The extent assigned to such equivalent region is the sum of the extent of the low pressure regions which compound the pattern:

$$\theta_{i,k}^- = \sum_{kp=1}^{QP} \theta_{i,kp}^-$$

where QP is the number of low pressure region in the pattern. Its equivalent circumferential intensity is defined as the extent-weighted value of the component regions:

$$(\Delta P_C/P)_{i,k} = \frac{\sum_{kp=1}^{QP}\left[(\Delta P_C/P)_{i,kp}\theta_{i,kp}^-\right]}{\sum_{kp}^{QP}\theta_{i,kp}^-} \qquad (11)$$

The radial total pressure distortion in the SAE standard is also defined in a ring-by-ring basis and is calculated from the difference between the average total pressure of the ring i $\overline{p0}_i$ and the average of the whole AIP ($\overline{p0_{AIP}}$):

$$(\Delta P_R/P)_i = \frac{\overline{p0_{AIP}}-\overline{p0}_i}{\overline{p0_{AIP}}} \qquad (12)$$

A positive value of $(\Delta P_R/P)_i$ indicates a pressure deficit for the ring i. Unlike CDI and RDI, the SAE descriptors provide a radial distribution of distortion parameters rather than a single value. For this reason $max(\Delta P_C/P)$ and $\overline{\Delta P_C/P}$ are defined as:

$$max(\Delta P_C/P) = max_{i=0,\dots,4}(\Delta P_C/P)_i \qquad (13)$$

$$\overline{\Delta P_C/P} = \frac{1}{5}\sum_{i=0}^{4}(\Delta P_C/P)_i \qquad (14)$$

The maximum radial distortion $max(\Delta P_R/P)$ and its average value $\overline{\Delta P_R/P}$ are also similarly defined. The peak value of intensity $max(\Delta P_C/P)$ indicates the maximum distortion intensity applied to a blade, independently of the radial position, which is a useful conservative parameter in a first assessment of inlet/engine compatibility, in particular to prevent stall. The average value of intensity $\overline{\Delta P_C/P}$ is an indicator of the overall variation of load applied to the blade, and is more useful for structural assessments.
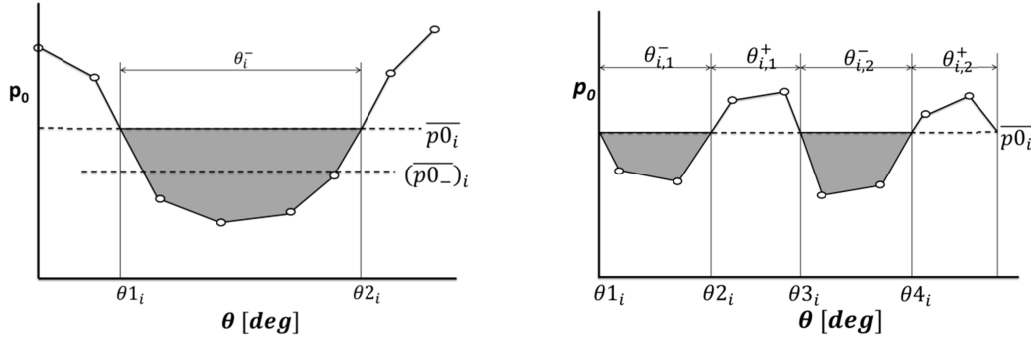

Figure 4: Definition of total pressure circumferential distortion extent and intensity for a generic ring i. [21]

E. Swirl distortion descriptors

Elements to quantify swirl distortion are outlined in the SAE report[2] where the definition of swirl intensity SI, swirl directivity (SD) and swirl pairs (SP) are provided. These descriptors are based on the swirl angle distribution on a ring-by-ring basis similar to the approach for total pressure. The swirl angle is defined as the circumferential angle from the axial direction of the velocity vector:

$$\alpha = tan^{-1}\left(\frac{v_\theta}{w}\right) \qquad (15)$$

The sign of α is usually defined relative to the engine rotation direction and is considered as positive if co-rotating. As for total pressure distortion the swirl angle distribution is divided in positive and negative angle regions and the swirl sector elements are defined as:

$$SS_i^+ = \frac{1}{\theta_i^+} \int_{\theta_i^+} \alpha(\theta)_i \, d\theta \tag{16}$$

$$SS_i^- = \frac{1}{\theta_i^-} \int_{\theta_i^-} \alpha(\theta)_i \, d\theta \tag{17}$$

which represents the average positive and negative angle respectively. In this work the compressor is not considered so a positive angle is defined as in the counter-clockwise direction looking at AIP from downstream. The average of the absolute value is defined as swirl intensity SI:

$$SI_i = \frac{SS_i^+ \theta_i^+ + |SS_i^-| \theta_i^-}{360} \tag{18}$$

The peak and average values of SI radial distribution ($max(SI)$ and $\overline{SI}$) are defined similarly to $max(\Delta P_C/P)$ and $\overline{\Delta P_C/P}$:

$$max(SI) = max_{i=0,\dots,4}(SI)_i \tag{19}$$

$$\overline{SI} = \frac{1}{5}\sum_{i=0}^{4}(SI)_i \tag{20}$$

F. Data processing
It is typical in intake distortion experimental work to evaluate the flow field at the AIP using a total pressure rake which comprises 8 circumferential rakes each with 5 radial probes. The probes are positioned across the AIP so that they are appropriately spaced for area-averaging purposes. Although the computational studies provide a substantially greater spatial resolution, for some of the integral results presented herein the data is sampled at 40 individual locations to enable comparisons with the experimental data which was acquired on a conventional 8x5 rake. For the flow field, spectral and POD analysis the full computed flow field is used. A spectral analysis of the flow field at the AIP is performed, where the Fourier transform is applied to the p_0 signal of every point of the plane. The frequency content is non-dimensionalized to Strouhal number (St) based on the AIP diameter and area-average axial velocity ($St = f D_{AIP}/\overline{W_{AIP}}$). Six St intervals of about 0.14 are defined from frequency intervals of 100 Hz based on the AIP diameter and the axial velocity from S-Duct 2A case, as outlined in Table 3. For every interval the inverse Fourier transform is applied to the frequency content at every point after the content outside the interval is set to zero. Finally, the standard deviation of the reconstructed signal is calculated. For a better understanding of the nature of the flow-field oscillations, the spectral analysis is encompassed with coherence and phase analysis, obtained from the Fourier transform of the cross-correlation of the total pressure at two distinct points at the AIP assessed across the time history of the simulation.

Table 3 Strouhal number bands definition based on S-duct 2A.

band	f [Hz]	St
1	0-100	0.0-0.14
2	100-200	0.14-0.28
3	200-300	0.28-0.43
4	300-400	0.43-0.57
5	400-500	0.57-0.71
6	500-600	0.71-0.86

IV. Results

A. Comparison with experimental results

To validate the numerical method for dynamic distortion simulations, a comparison has been performed with the qualitative and quantitative experimental data provided in Delot et al[9,11]. In contrast with the geometry used to assess the impact of H_o/L, Ma and Re, the geometry of the Delot et al experiment[9] has a spinner downstream of the AIP and a shorter inlet duct. The validation is performed for low Mach number, as in S-Duct 2B, where both experimental static distortion parameters of total pressure and spectral distribution of total pressure fluctuations are reported by Delot et al[9]. Such experimental data are compared with the S-Duct 2BS case which uses the geometry from the experiment, including the spinner, and the inlet cross-sectional total pressure distribution.

A comparison of the time averged static distortion (Table 4), shows that there is reasonable agreement between the computations and the experiment. The pressure recovery is in excellent agreement and overall the other distortion metrics are typically within 10-15% of the reported measured values. The distribution of the pressure recovery at the AIP2 similarly shows good agreement in the levels and extent of the total pressure loss regions at the duct exit (Fig. 5). The DDES calculations show the characteristic loss region at the bottom of the duct although the simulations very slightly over estimate the loss relative to the measurements. Although the distribution of total pressure ratio is very similar between the CFD and experiment and the overall loss is identical, the differences in the distortion metrics are a little higher. The CFD results are symmetric although the experimental data shows a slight asymmetric in the upper regions. This highlights the sensitivity of the distortion parameters to small local changes. A key element of the current work is in the evaluation of the unsteady aspects of the flow field. A spectral analysis of total pressure from the computational and experimental data highlights the flow characteristics at different frequencies (Fig.6). Overall there are distinct regions in which the total pressure fluctuations have clear dominant distributions at particular frequency bands and there are some notable aspects evident in both the computational and experimental data. At the lowest frequency of 0-100Hz both the CFD and experiments indicate a local maximum towards the spinner. In addition, both datasets clearly show the maximum unsteadiness in the regions associated with the time-averaged positions of the primary contra-rotating secondary vortices. The CFD indicates slightly higher levels of unsteadiness although the topology is in good agreement with the measurements. At the higher frequency bands the unsteadiness again becomes centrally positioned and the levels gradually decay with increasing frequency. Overall the spectral results indicate that the DDES calculations are capturing the main time-averaged and unsteady aspects of the flow.

Table 4 Comparison of static distortion between spinner case, S-Duct 2BS, and experimental data[9]

S-duct	$\overline{PR}_{<p0>}$	$DC60_{<p0>}$	$CDI_{<p0>}$	$\overline{\Delta P_C/P}_{<p0>}$	$max(\Delta P_C/P)_{<p0>}$	$RDI_{<p0>}$	$\overline{SI}_{<p0>}\ deg$
2BS AIP2	0.993	0.327	0.0143	0.0060	0.0074	0.0083	2.01
2BS Exp AIP2	0.993	-	0.0126	0.0051	0.0065	0.0070	-

Table 5 Summary of time-averaged static performance and static distortion metrics at the AIP section.

| S-duct	$\overline{PR}_{<p0>}$	$DC60_{<p0>}$	$CDI_{<p0>}$	$RDI_{<p0>}$	$\overline{\Delta P_C/P}_{<p0>}$	$max(\Delta P_C/P)_{<p0>}$	$\overline{SI}_{<\alpha>}$
1 DDES	0.973	0.265	0.036	0.033	0.015	0.020	1.86
1 RANS	0.970	0.493	0.059	0.021	0.028	0.037	2.09
2A DDES	0.969	0.354	0.047	0.032	0.019	0.025	1.77
2A RANS	0.968	0.519	0.060	0.022	0.030	0.040	2.31
2B DDES	0.993	0.280	0.011	0.009	0.004	0.005	1.86
2B RANS	0.992	0.466	0.016	0.006	0.007	0.010	2.14
3A DDES	0.947	0.242	0.058	0.030	0.024	0.034	3.12
3A RANS	0.947	0.175	0.059	0.040	0.027	0.037	6.02
3B DDES	0.988	0.156	0.013	0.008	0.005	0.007	2.59
3B RANS	0.988	0.159	0.014	0.008	0.006	0.008	5.73
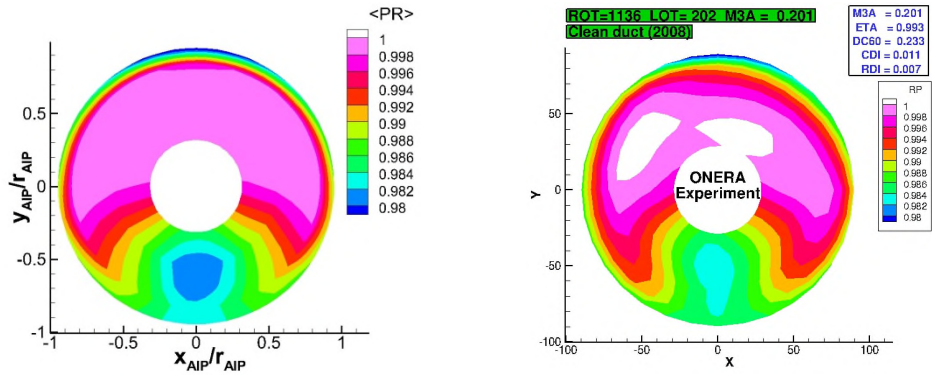
Figure 5 Calculated DDES time averaged pressure recovery comparison between S-Duct 2BS (left) and experiment (right)[11] at the AIP2 section.
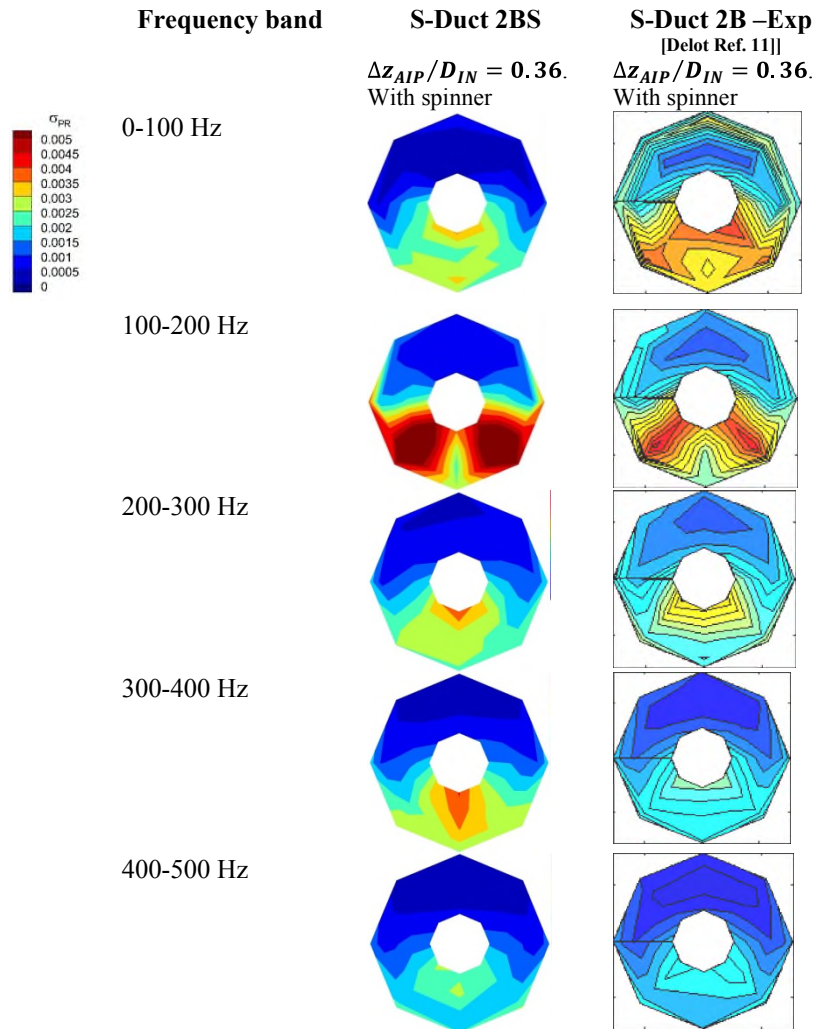

Figure 6 Comparison of total pressure spectral bands for S-Duct 2BS DDES calculations (left) and measurements (right) [11] with $Ma_{CL} = 0.28$ at the AIP2 section.

B. Time averaged and statistical parameters

For the five configurations considered in this study the time-averaged values of the key descriptors are calculated at the AIP section at a distance $0.5D_{in}$ from the S-Duct outlet as in Fig. 1. A comparison with the results from the RANS simulations is also provided (Table 5, Fig. 7). Not surprisingly the average pressure recovery is lower for the Duct-3 configurations due to the higher offset, and there is a slight benefit of the high Reynolds number when comparing Duct 1 and Duct-2A. However, the DDES DC60 levels are higher for the Duct-2 configurations when compared with the more aggressive Duct-3. This is because for the Duct-3 cases although the loss in total pressure is greater and over a larger region (Fig. 8), it is more centrally located and the DC60 parameter is constructed so that this results in a lower measure of distortion. It is also notable that there is a substantial difference in the DC60 levels between the RANS and DDES calculations for Duct-2 with the RANS levels being notably higher. Duct-3 is less different and the RANS calculations are broadly in good agreement with the DDES. CDI and RDI are less sensitive to the differences between the RANS and DDES although the differences generally increase with Mach number. It is also of note that the RANS calculated swirl intensity for Duct-3 is almost twice the level of the DDES solutions. Overall it indicates that even for the time-averaged properties, although the average PR may be calculated relatively well by the RANS simulations, there can be notable differences in the more complex distortion descriptors.
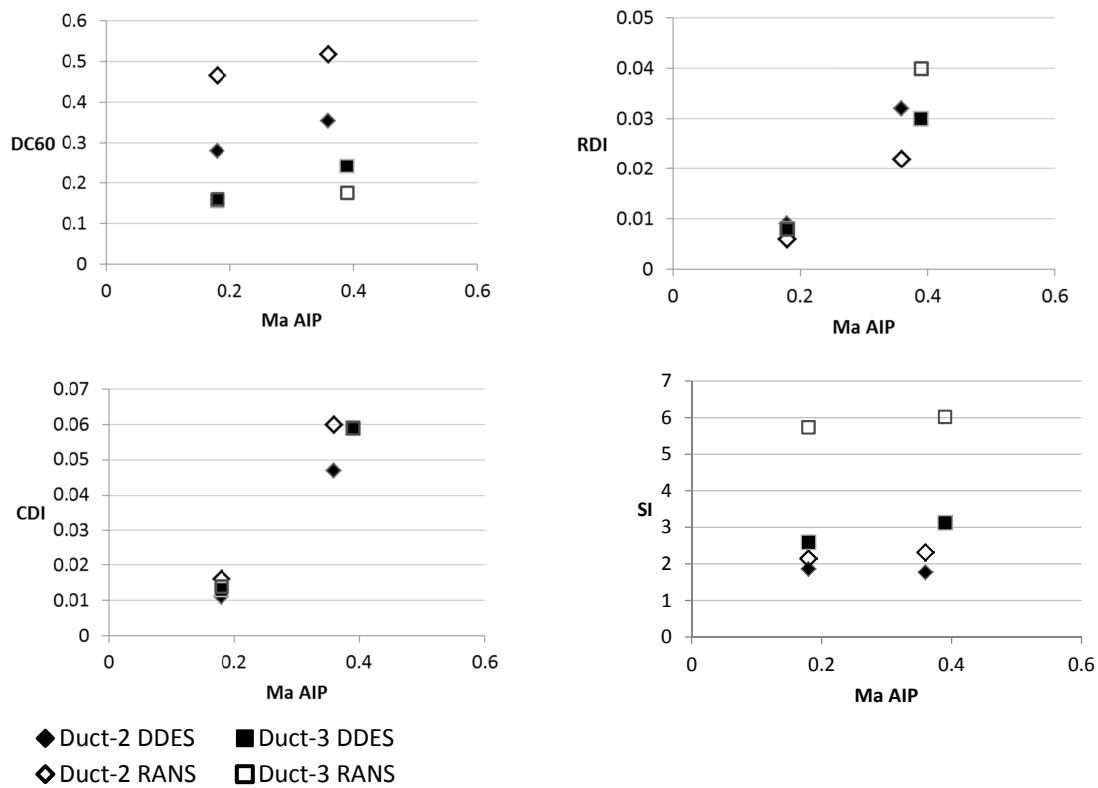

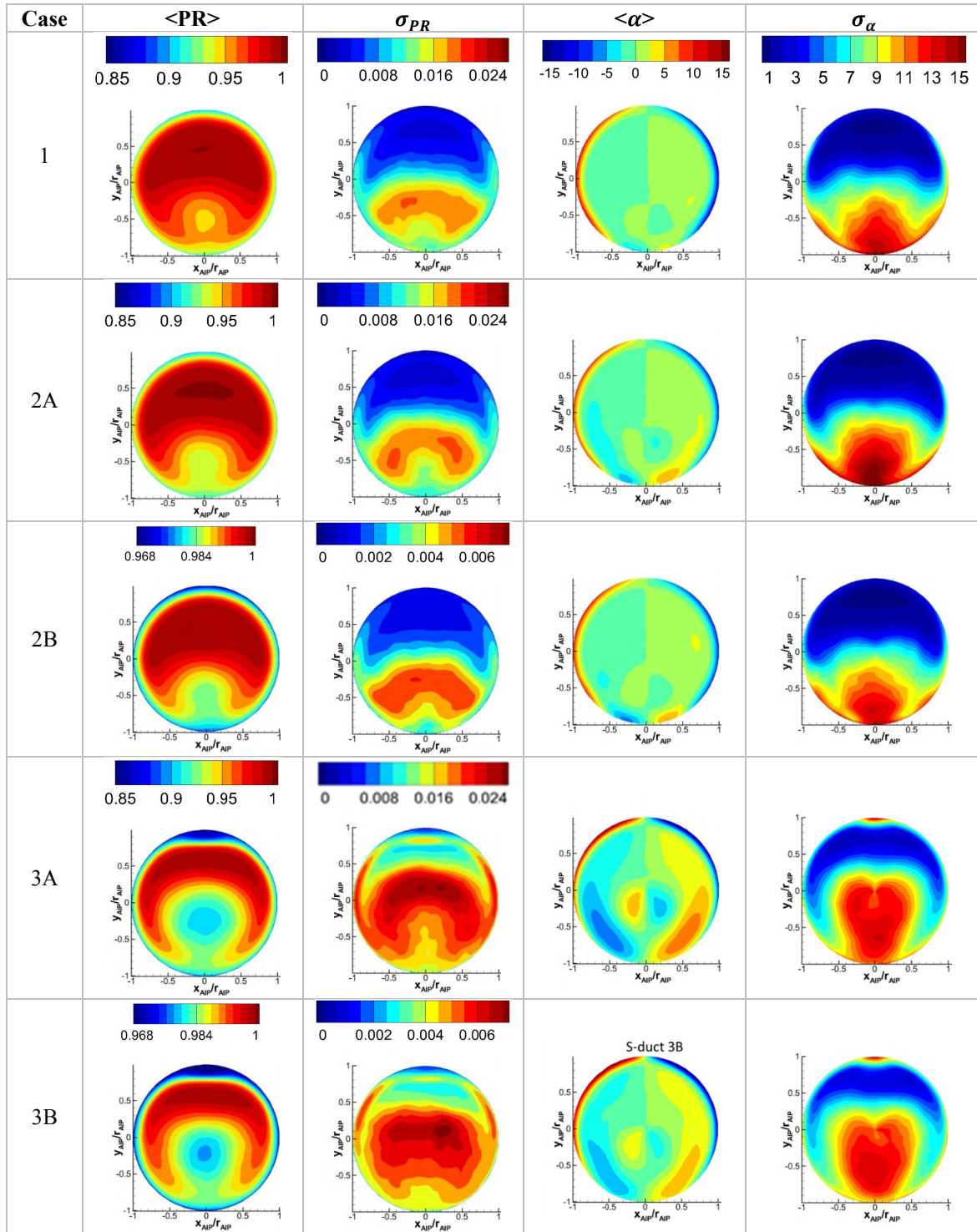**Figure 7 Comparison of distortion metrics for RANS and DDES calculations at the AIP section**

Figure 8 Calculated pressure recovery and swirl at the AIP section. Time averaged and standard deviation.

Fig. 8 illustrates the time-averaged and standard deviation distribution of the swirl angle α at the AIP section as shown in Fig 1. Notable effects are observed due to the effect of the non-dimensional S-duct offset and when H_o/L is increased from 0.268 (S-Duct-2) to 0.493 (Duct-3). The time-averaged location of the twin vortices move toward the central part of the AIP and their effect is extended to an upper region of the plane. The main total pressure loss

region also moves to a more central position and the region of maximum total pressure unsteadiness is mainly associated with the upper bounds of this loss region for both Duct-2 and -3. For the higher offset configuration (Duct-3), the peak value of $<\alpha>$ increases from 12° to 20°. However, there is a slight reduction in the swirl fluctuations σ_α for Duct 3 and the distribution is more centrally positioned. The reduction in unsteady swirl for the more aggressive duct is of note as it is different from the effect on total pressure and, due to the radial movement of the main streamwise vortices, the centreline separation and the secondary flow vortices become more intertwined with a damping of the swirl unsteadiness.

C. Flow distortion characteristics

The distortion statistics are summarized in Table 6. There are a number of sensitivities worth highlighting. For example, the effect of Reynolds number for the low-offset configuration shows that there is generally a very small reduction in the unsteady distortion metrics when the Reynolds number is reduced from 2.6×10^6 to 1.7×10^6 for Duct 1 and Duct 2A. Also of general note is the very high levels of unsteady swirl with average SIs in the region of 6-9° but with an area averaged maximum SI of up to 16.4° for Duct-3A. This is a notably high level. The effect of Mach number for both Duct-2 and -3, shows that there is a large reduction in the steady and unsteady CDI and RDI which increase with M, but that in general the other parameters are unaffected. The most notable changes arise due to the change in geometry from Duct-2 to the higher offset Duct-3. Interestingly the $<DC60>$ reduces for the higher offset but the swirl based parameters $<SC60>$ and SI increase. Broadly CDI and RDI are unaffected which highlights the limitations of only considering time averaged total pressure based distortion metrics. The most notable impact on the unsteady distortion is at the higher Mach number (-2A and -3A) where the deviation of RDI doubles with the increase in offset. Overall these results highlight the importance of considering both the unsteady distortion aspects as well as the swirl based descriptors. It also indicates that the characteristics are relatively insensitive to Reynolds number, but that there are notable Mach number sensitivities for the unsteady total pressure as well as the RDI and CDI metrics.

Although the statistics of the key distortion descriptors RDI and CDI (Table 6) highlight significant differences between the different duct configurations, it is also useful to consider the unsteady aspects of these metrics in more detail. Within this context the simultaneous distributions of RDI and CDI are of interest (Fig. 9). For Duct 1 there is a relatively clustered distribution of points in a range of variation of CDI of about 0.09 and a variation of RDI of about 0.03. In comparison with the datum Duct 1 configuration, Duct 2A is the same geometric shape but at a lower inlet diameter and therefore the Reynolds number ($Re_{Din}=1.7 \times 10^6$) is also reduced. Overall the RDI-CDI map is similar, but the range of CDI is slightly truncated and it is also of interest to note the excursion of occasional instances of relatively high values which are over twice the time averaged value. For Duct 2B where the Mach number is reduced from 0.36 to 0.18, there is a dramatic reduction in the distortion coefficients where they are generally 3 to 4 times smaller than the results for Duct 2A at Ma=0.36 due to the nature of the definition of CDI and RDI and the notable change in the $<PR>$. For the S-Duct 3 configuration where the S-duct offset H_0/L is increased from 0.268 to 0.493, there is an increase in both the time averaged RDI and CDI distortion levels as well as an increase in the extreme values. With this more aggressive duct, there is a more notable scatter in the RDI distribution in particular where the standard deviation of RDI has almost doubled from approximately 0.006 to 0.013. These lower frequency extreme distortions are of interest as these events may be a key consideration in the transient response of the compression system and the ultimate effect on surge margin.

The nature of the unsteady aspects on the swirl and total pressure distortions is illustrated in the SC60-DC60 maps (Fig.9). For Duct-1 and Ducts-2A and -2B, both the SC60 and DC60 show notable levels of variation relative to the mean values and clealy highlight the low frequency, but high distortion, events that occassionally occur. For example, Duct-2A shows that the peak SC60 and DC60 are about twice the mean levels. For these ducts, although there is evidence of a correlation between the SC60 and DC60, it is relatively weak and it more importantly highlights the importance of considering both the swirl and pressure distortions simultaneously. For example, at a mean $<SC60>$ of around 0.2 the DC60 excursions range from about 0.15 to 0.75. Similarly, the SC60 ranges from about 0.1 to 0.4 for a mean $<DC60>$ of 0.43. The impact of the higher offset for Duct-3A resulted in an increase in the unsteady RDI. In contrast, for this more aggressive duct the unsteady aspects of the SC60 and DC60 metrics are notably reduced. This is partially reflected in Fig. 8, where the unsteady swirl takes a more central position and the levels are reduced relative to the less aggressive Duct-2. The same characteristics and differences are obversed at both Mach numbers. Overall it highlights the complexity of the problem, the importance of both the steady and unsteady aspects, and the relative independence of the swirl and pressure based metrics.
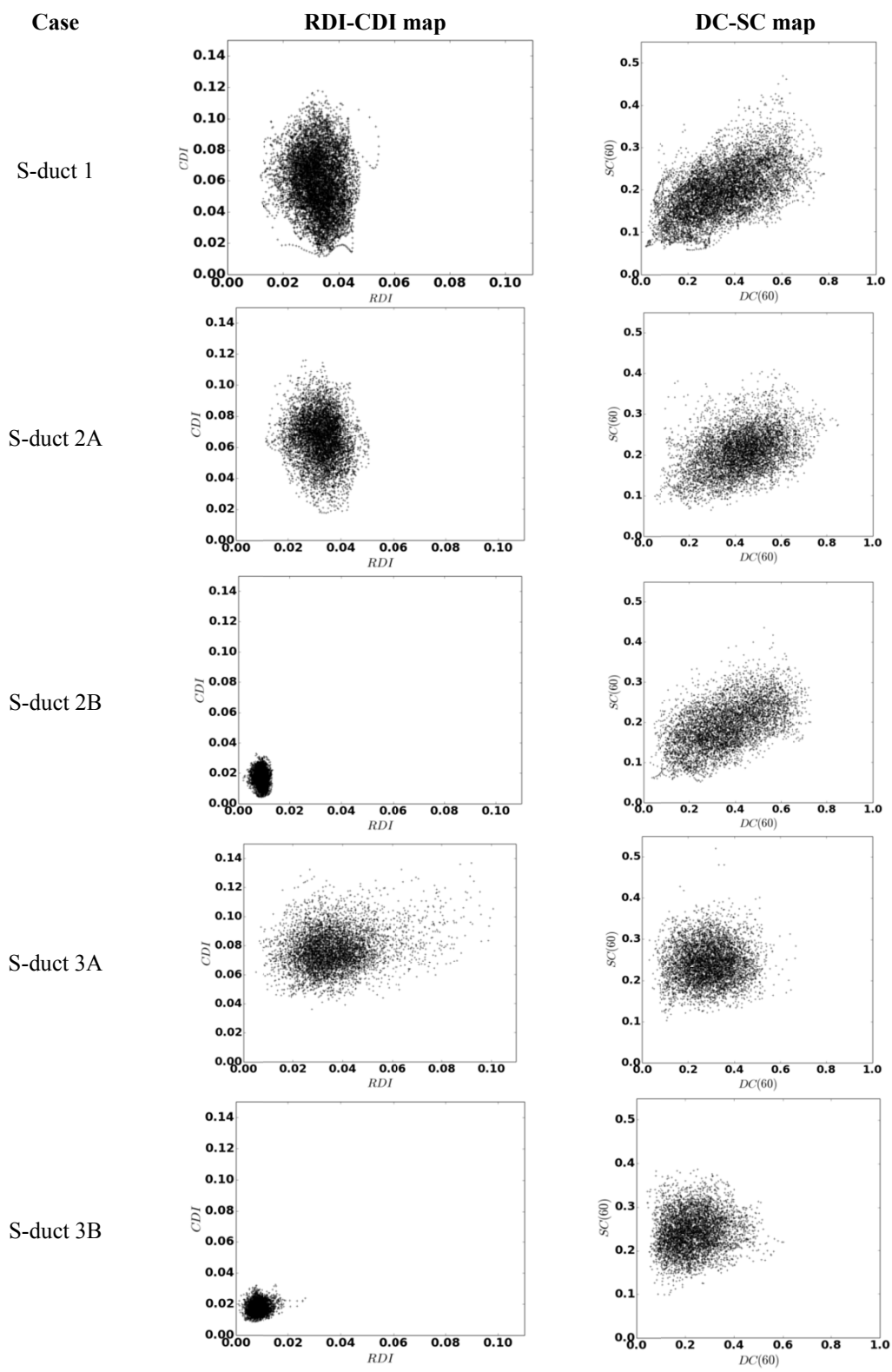
Case	RDI-CDI map	DC-SC map

S-duct 1

S-duct 2A

S-duct 2B

S-duct 3A

S-duct 3B

Figure 9 Distortion metric maps from DDES temporal snapshots at the AIP section

Table 6 Summary of DDES calculated distortion statistics

	PR	CDI	$\overline{\Delta P_C/P}$	RDI	DC(60)	SC(60)	$\overline{SI}\ deg$
S-duct 1							
<.>	0.9728	0.059	0.023	0.033	0.348	0.198	6.0
σ	0.002	0.019	0.009	0.006	0.149	0.059	1.9
max	0.034	0.118	0.050	0.054	0.781	0.470	14.0
S-duct 2A							
<.>	0.969	0.066	0.027	0.032	0.426	0.207	6.2
σ	0.003	0.015	0.008	0.006	0.131	0.052	1.7
max	0.040	0.116	0.052	0.051	0.849	0.410	13.1
S-duct 2B							
<.>	0.993	0.017	0.007	0.009	0.362	0.193	5.8
σ	0.001	0.005	0.002	0.002	0.144	0.057	1.8
max	0.010	0.033	0.013	0.013	0.732	0.436	12.7
S-duct 3A							
<.>	0.947	0.077	0.033	0.036	0.289	0.243	8.3
σ	0.003	0.014	0.006	0.013	0.099	0.047	1.8
max	0.067	0.137	0.052	0.101	0.668	0.521	16.4
S-duct 3B							
<.>	0.988	0.018	0.007	0.009	0.233	0.243	8.5
σ	0.001	0.004	0.001	0.002	0.091	0.045	1.8
max	0.015	0.033	0.012	0.027	0.602	0.388	14.8

D. Flowfield Spectral Analysis at the AIP

For the DDES calculations, the unsteady flow field at the AIP has been analysed and the distribution of the total pressure fluctuations σ_{PR} divided in Strouhal number bands of about 0.143 presented for S-Duct 1, S-Duct 2 and S-Duct 3 (Fig. 10). Overall for these configurations there are distinct regions in which the total pressure fluctuations have clear dominant distributions at particular Strouhal numbers. For Ducts-1, -2A and -2B, the most dominant feature is in the Strouhal range of 0.29 to 0.43, where there are the two distinct symmetric peaks in the region around the time averaged location of the classical streamwise secondary flow vortices. The levels are almost the same with only a slight reduction in the peak values for the higher Reynolds number Duct-1. Although there are central regions of unsteadiness at lower St, the second most notable aspect is the relatively high leves of unsteadiness in the centre of the AIP which arises at St=0.57-0.72 and St=0.72-0.86, for Ducts-2A and -2B, respectively. This higher frequency unsteadiness is more associated with the centerline shear layer separation.

A more notable difference arises for Ducts-3A and -3B. Although the Mach number and Reynolds number are similar to Duct-2A and -2B, the offset has increased from H_o/L=0.268 to 0.493 and the unsteady flowfield distributions are different. In general the unsteadiness is more centrally located in agreement with the changes observed for the time averaged total pressure ratio (Fig. 8) and the main unsteadiness now arises at a higher St range across 0.43-0.72. The clear characteristics associated with the symmetric secondary flows is still evident, but are much less distinct. There is also evidence for Duct-3A and -3B of a central region of unsteadiness but it also is less distinct. The changes in Reynolds number and Mach number change the level of unsteadiness, but have no notable impact on the Strouhal number distributions or characteristics. Overall the results indicate that the main total pressure unsteadiness is associated with changes in the secondary flow vortices as well as regions associated with the central streamwise separation. The indications are that at modest offset these events arise at difference frequency bands, but that as the duct becomes more aggressive the demarcation between these aspects becomes less clear.

To help to understand the underlying nature of the flow unsteadiness, an assessment of the cross correlation within different parts of the flow field has been considered. For Duct 2A, a cross-correlation of the unsteady total pressure at the peak location of unsteadiness associated with the time-averaged vortex positions has been performed (Fig. 11). The coherence shows that there are two main frequencies of interest at approximately 260Hz and 540Hz. The phase characteristic shows that the unsteadiness at 260Hz is approximately -170° out of phase while the

unsteadiness at 540Hz is relatively in phase. Taken in conjunction with animations of the flow field topology this indicates that there is a circumferential oscillation associated with the secondary flows as well as a different mechanism associated with the high frequency in-phase unsteadiness in the centre of the AIP. Analysis of the flow field indicates that this is associated with the streamwise flow separation more along the duct centreline. Similarly, for Duct 2B, the coherence shows that there are two main frequencies of interest at approximately 115Hz and 230Hz (Fig. 12). The phase characteristic also shows that the unsteadiness at 115Hz is approximately 170° out of phase while the unsteadiness at 230Hz is relatively in phase. This is the same as for Duct-2A.just that the frequencies has changed in line with the lower Mach numbers and velocities. For Duct 3, the spectra are more distributed and the phase characteristics are not as distinct (Fig. 13). There is a maximum in the range 400-500Hz but there is a notable amount of more broadband unsteadiness. In this context is it surmised that secondary flows of the more aggressive Duct 3 are still present but that they are positioned in a more central location and that they are more merged with the unsteadiness associated with the centreline separations and are more difficult to discern.
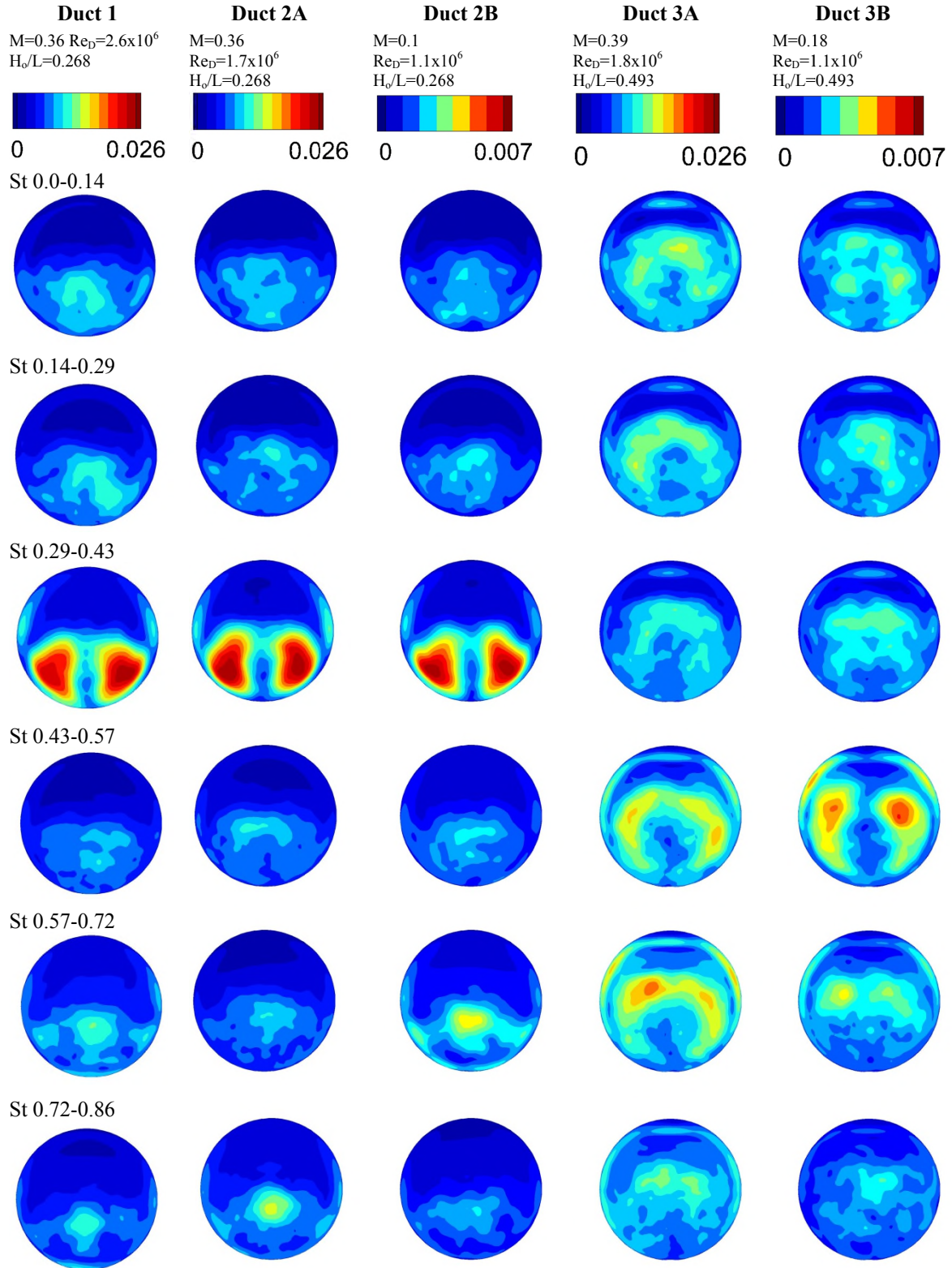
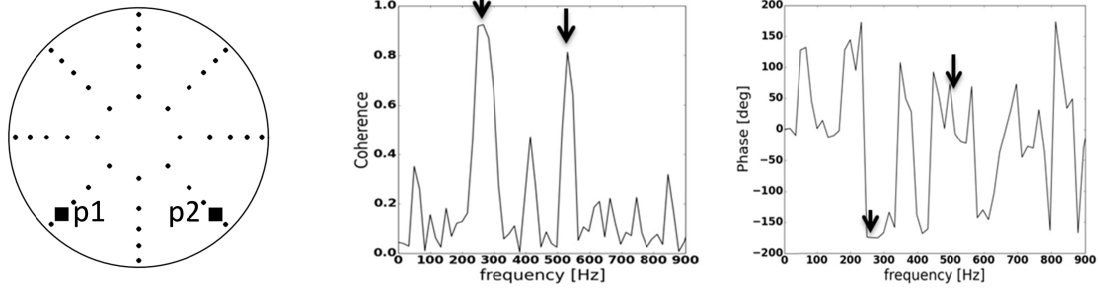**Figure. 10 AIP spectral distribution of total pressure fluctuations**

Figure 11 Coherence and phase distribution between two opposite points on the AIP. S-Duct 2A.
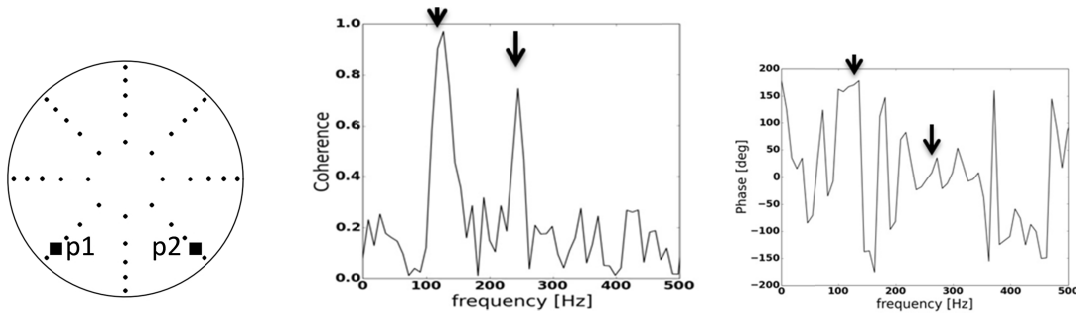

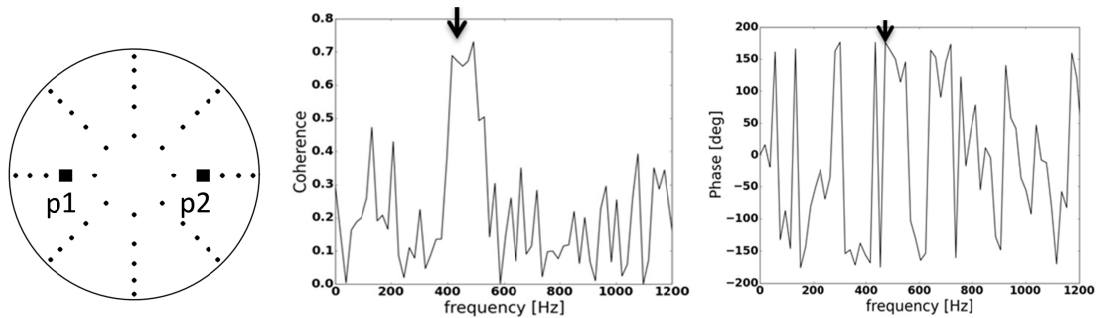**Figure 12 Coherence and phase distribution between two opposite points on the AIP. S-Duct 2B.**

Figure 13 Coherence and phase distribution between two opposite points on the AIP. S-Duct-3A.

E. Proper Orthogonal Decomposition

To develop a better understanding of the unsteady behaviour of the flow and the underlying flow structures, the use of the Proper Orthogonal Decomposition (POD) method was applied to the total pressure distribution at the AIP. The modes are sorted by the energetic content of their signal in descending order.

1. POD method

Turbulent flows are characterised by the existence of large-scale, deterministic, coherent structures, often obscured by random, small-scale turbulent fluctuations. Coherent structures are thought to account for most of the essential flow physics. Therefore identifying such flow features and understanding their dynamics have become major aims in turbulence research[24]. The Proper Orthogonal Decomposition (POD) has been widely utilised to extract dominant flow features and ultimately coherent structures. The POD has been recently applied for the

analysis of turbulent flows in very different applications, such as the flow in a backward-facing step[24,25], reciprocating internal combustion engines[26], turbulent boundary layers[27] and curved pipes[28].

A detailed mathematical description is beyond the scope of this paper, and only a brief review of the most basics aspects of the POD will be presented. For a more rigorous derivation, the reader is referred to Holmes et al[29]. Considering for simplicity a scalar field $u(x, y, t)$, the POD consists of finding an orthogonal basis $\{\varphi_j(x, y)\}$ that maximises the projection of u onto φ. The functions φ_j, often called POD characteristic modes, represent those flow features responsible for most of the signal energy in a statistical sense and may be, sometimes, associated with coherent structures. The POD representation of the original flow field is then obtained by a series of the POD characteristic modes, each of them being multiplied by a temporal coefficient[30] (Eq. 21)

$$u_k(x, y, t) = \sum_{j=1}^{k} a_j(t)\varphi_j(x, y) \tag{21}$$

The temporal coefficients are statistically uncorrelated and the modes are orthonormal. These properties permit to express the area-averaged mean-squared value of the scalar field as the series of the mean-squared value of the temporal coefficients (Eq. 22).

$$\langle \overline{u_k^2} \rangle = \sum_{j=1}^{k} \langle a_j^2 \rangle \tag{22}$$

To increase convergence of the reconstruction, the modal contributions in the series are ordered in decreasing order of the mean-square value of the associated temporal coefficient, which is often referred to as the modal energy. The term energy is widely utilised since POD has been historically applied to velocity fields, for which the mean-squared value of the coefficients represents the area-averaged mean kinetic energy accounted for each considered mode. Even though this terminology will be used in the present investigation, care must be taken when applying POD to total-pressure fields, since the squared-value of the pressure does not have units of energy. The main advantage of the POD reconstruction is its optimality in the sense that, for a given number of terms in the series, the area-averaged mean-squared value of the considered variable is approximated more accurately than in any other linear decomposition. If the variable of choice is the velocity vector field, then the POD maximises the kinetic energy content in the reconstruction[31]. In the present investigation the POD has been implemented utilising the method of snapshots, developed by Sirovich[32], which reduces the associated computational cost. This approach consists of obtaining the POD modes as $\varphi_j = \langle u\beta_j \rangle$, where β_j are the eigenfunctions of the correlation matrix, C(t,t') (Eq. 23). The temporal coefficients are then evaluated by projection of each mode, properly normalised, onto each snapshot of the original flow field (Eq. 24).

$$C(t, t') = \frac{1}{A} \int_A u(x, y, t')u(x, y, t)dA \tag{23}$$

$$a_j(t) = \frac{1}{A} \int_A \varphi_j(x, y)u(x, y, t)dA \tag{24}$$

2. POD analysis for total pressure

For Duct-2A (Ma=0.36) the distribution of the variance for the POD mode coefficients "a" ,as a percentage of the total variance content, for the first 10 modes shows that the content is mostly dominated by the first three modes with a subsequent gradual monotonic decrease (Fig. 14). Mode 0 is representative of the time-averaged total pressure distribution and modes 1, 2 and 3 show distinct spatial mode distributions (Fig. 15). Mode 1 has an anti-symmetric arrangement indicative of the underlying streamwise vortices associated with the secondary flows. As the POD coefficients are anti-symmetric it supports the evidence from the cross-correlation analysis at these locations which indicates an out of phase oscillation of the main flow features in this area. This is further supported by considering a frequency analysis of the POD coefficients for mode 1 (Fig. 17) which shows that the primary Strouhal number associated with mode 1 is around 0.4. The banded frequency spectrum for Duct 2A also shows that the total pressure unsteadiness is dominated in this region of the mode 1 maxima within the Strouhal range 0.29-0.43 (Fig. 10). Mode 2 is shown to have a symmetric distribution with the local maximum located in relatively central position. A frequency analysis of the POD coefficient for mode 2, shows a clear peak at around St=0.75 (Fig. 17) which also agrees with the spectrum peak within the Strouhal range 0.72-0.86 (Fig. 10). The assessment for Duct-2B when the Mach number reduces to 0.18 shows that the POD energy distribution is almost the same as the reference Duct-2A configuration where the distribution is clearly dominated by modes 1 and 2 followed by a gradual reduction for the higher modes (Fig.14). Similarly, the mode shapes are relatively insensitive to the effect of Mach

21

number with very little difference noted in modes 0-2 and minor differences observed in modes 3-5 (Fig. 15). For Duct-2A, by considering the spectrum of the POD coefficients, mode 1 is also noted as an asymmetric out of phase mode with a primary Strouhal number of around 0.4 and mode 2 is a symmetric unsteady mode within the duct centre at a Strouhal range 0.57-0.72 (Fig. 10). These are similar to the spectral distributions shown in shown in Fig. 10. Overall, the POD aspects of the flow field are primarily unaffected by the change in Mach number.

The characteristics for Duct-3A and -3B are notably different to Duct-2 as initially illustrated in the spectral distributions (14). The POD energy distribution shows that, relative to Duct-2A and -2B, for Duct-3A and 3B mode 1 is much less distinct and the energies drop from around 27% to 15%. For Ducts -3A and 3B the energy distribution is flatter relative to Ducts -2A and 2B although beyond mode 3 the distributions are broadly similar. The more detailed characteristics of the modes show distinct differences between Ducts-2 and Ducts-3. For Duct-3B the structures for modes 0-3 (Fig. 16) are generally similar to those for Ducts-2A and 2-B (Fig. 16). There are some topological differences such as the clear radial movement in the centres of mode 1 as well as a shift in position for modes 2 and 3. For modes 4 and 5 the distributions are clearly different between those of Ducts-2A, -2B and that shown for Duct 3B. For Duct-3A there are a few notable differences in comparison with Duct-3B and the effect of Mach number is not negligible. The geometry is the same for both of these configurations, but the AIP Mach number is 0.36 for -3A and 0.18 for -3B. The first difference is in modes 1 and 2 where for -3B these modes comprise an anti-symmetric shape and a single local maximum shape, respectively (Fig. 16). In comparison at the higher Mach number of 0.36, these modes are reversed with the centre symmetric topology now comprising mode 1. Mode 3 and mode 5 are broadly the same for Duct-3A and 3B and there is a clear inversion of the distribution of local maxima and minima for mode 4. A frequency analysis of the POD mode coefficients shows that for Duct 3A, mode 2 has a clear strong peak at about St=0.6 although there is a relatively wide range of spectral content. Mode 1 exhibits two split spectral peaks at about St=0.5 and 0.7. Overall this is consistent with the distribution of pressure spectral analysis (Fig. 10) and indicates that the unsteadiness for Duct-3A is associated with a range of less distinct modes of a more amalgamated nature. This is because of the stronger secondary flows which results in the primary streamwise vortices separating in a more aggressive manner and migrating into a more central position. In addition, the centreline region is dominated by the classic diffusion separation which is associated with unsteady vorticity orthogonal to the r-θ plane and overall these two separated flows are of a more amalgamated nature. This is notably different from the characteristics of Duct-2A in which these two flow features are very distinct in location and frequency. For Duct-3B the characteristics are slightly different again. There is a clear single strong peak at about St=0.55 which is associated with mode 1 although there are also other smaller local maxima at sub-harmonics of about 0.18 and 0.36 (Fig. 17). There is also a secondary spectral peak for modes 2 and 3 at around St=0.85.
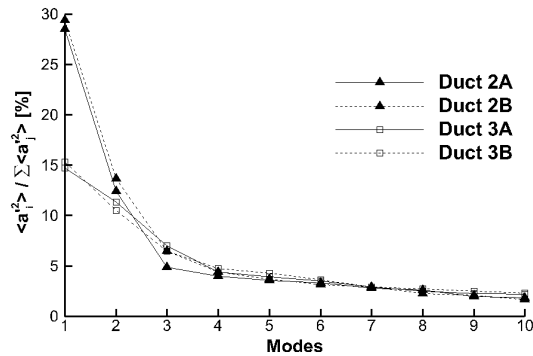

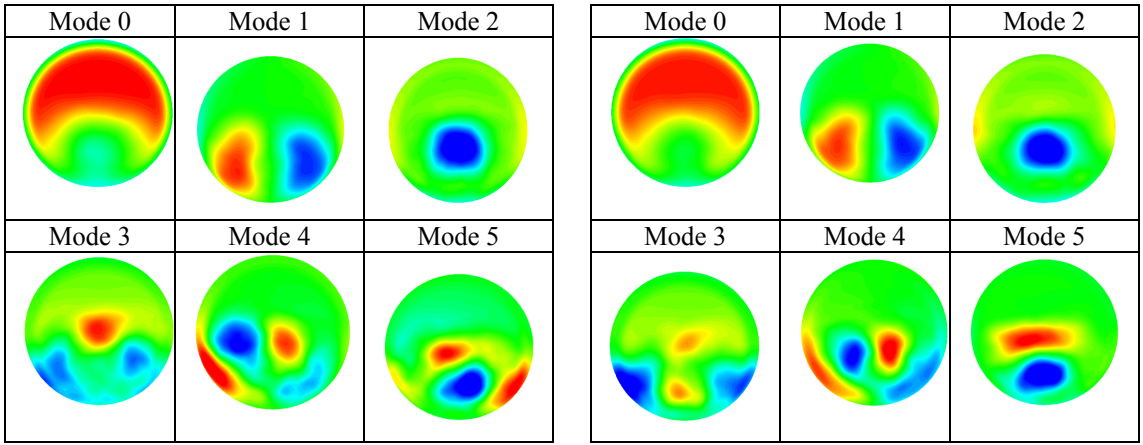**Figure 14 POD coefficients for Po variance for mode 1 to 10 distributions at the AIP**

Figure. 15 AIP plane distribution of POD modes 0 to 5 for the cases S-Duct 2A (left) and 2B (right)
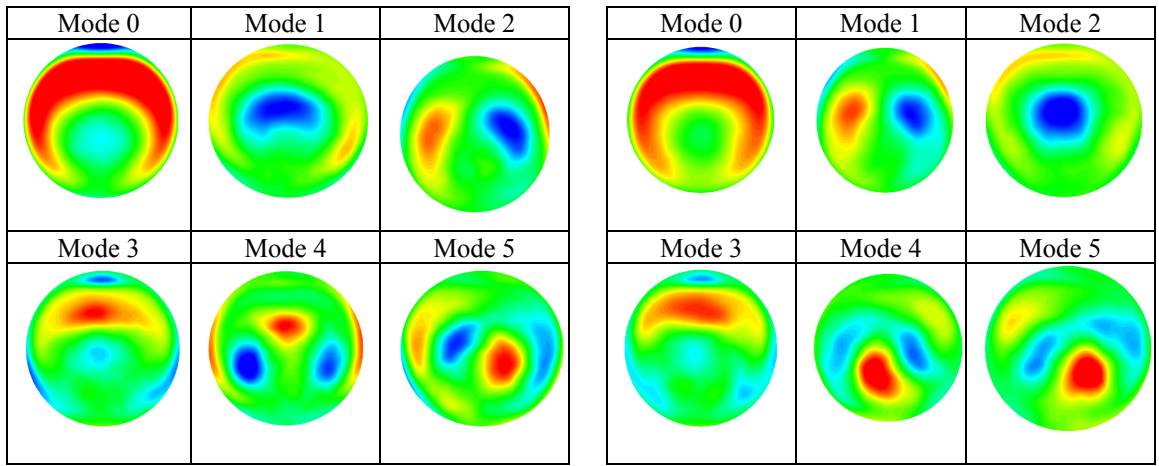

Figure. 16 AIP plane distribution of POD modes 0 to 5 for the cases S-Duct 3A (left) and 3B (right)
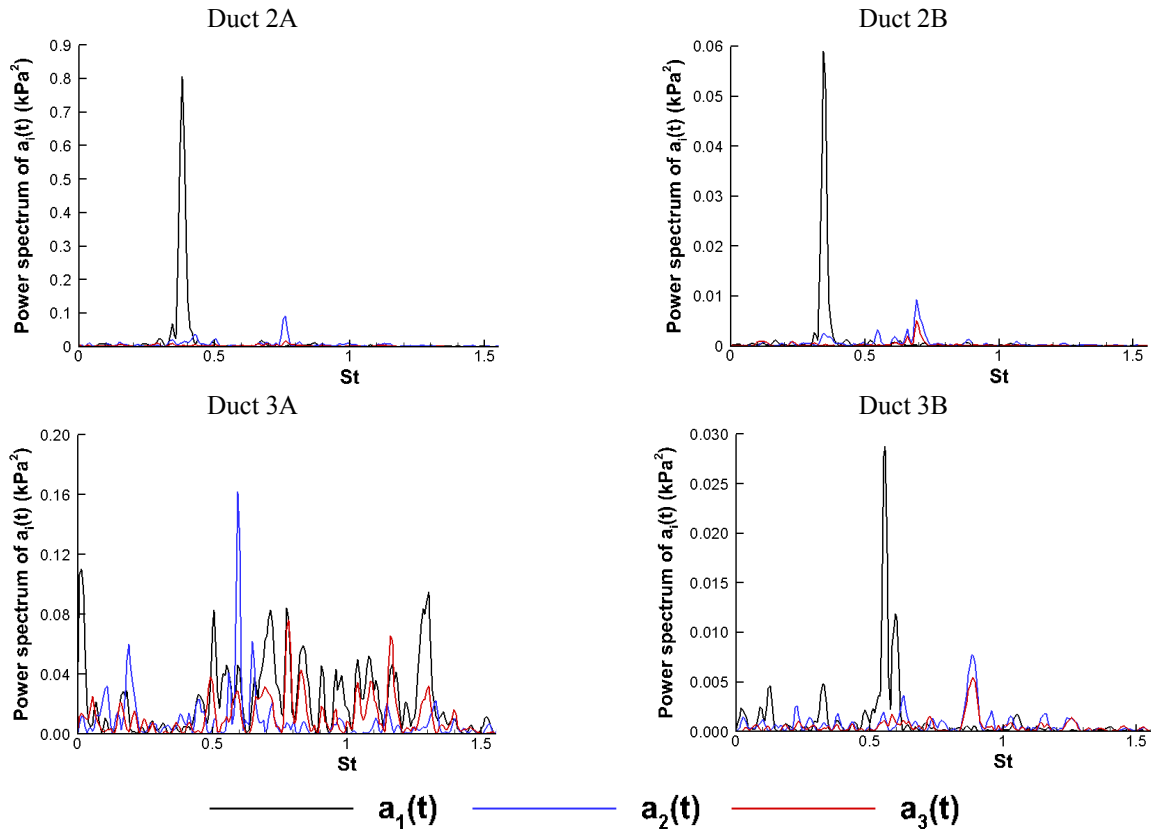
Figure 17 Spectral distribution of the total pressure POD coefficients.

3. Effect of POD modes on flow distortion

Additional information on the relative importance of the POD modes for the time-averaged and dynamic aspects of the flow distortion metrics is also of interest. This is particularly pertinent for the CDI-RDI metrics which exhibit notable levels of standard deviation (Fig. 9). The impact of the individual POD modes was evaluated by reconstructing the AIP flow field snapshots for all the POD modes with the cumulative range of mode of interest omitted. This enabled the time history and statistics of the distortion metrics to be calculated for the time-series and the overall effect on the time-averaged and distortion metric statistics to be quantified. The first assessment considered the impact of just mode 0 on the steady distortion metrics by solely reconstructing the flow field based on this mode and then calculating the distortion metrics (Table 7). Typically mode 0 accounts for about 90% of the RDI when compared with the full signal. The exception is Duct-2A where it is slightly lower at about 83%. The CDI is less dominated by the single mode 0 and it typically accounts for 65-75% of the CDI steady distortion levels.

The influence of the higher modes on both the time-averaged and unsteady CDI and RDI metrics is also considered. This is assessed by evaluating the unsteady reconstructed flow field based on the cumulative removal of the modes. For the average CDI, there is a monotonic reduction in <CDI> and gradually more modes from 1 to 10 are reduced. Duct-2B shows that mode 1 has the biggest initial effect where the <CDI> reduces to 85% of the full value but that the removal of the additional modes 2-10 only reduces it further to about 75%. The same general characteristic is observed for the other ducts with Duct-2A the least affected. The impact of the modes on the CDI standard deviation shows a broadly similar effect with a generally monotonic reduction in the CDI standard deviation as more of the modes are removed. As with the <CDI>, Duct-2 is more affected than Duct-3 and for Duct-2B, the unsteady CDI has reduced to about 50% when modes 1-10 are removed. For Duct -2A, the reduction with the number of modes is not exactly monotonic which highlights and interaction between the different unsteady modes on the CDI, but the effect is very small. Overall it shows that for the unsteady elements of the CDI distortion, it is not strongly dominated by a single mode. The time averaged RDI for Duct-2 shows almost no sensitivity to mode 1 and higher and is completely dominated by mode zero. This is mainly due to the nature of the definition of

24

the RDI term. For Duct-3A, the <RDI> shows that mode 1 has the main impact after mode 0 and that the higher modes play a negligible role. The contribution from modes 1 and higher to the time-varying area-averaged total-pressure is mostly negligible. Any influence on RDI is then dependent on the local circumferential average pressure, either on the inner or outer ring which for Duct-2 is always the outermost ring (Eq. 3). For Duct 2, although the anti-symmetric modes are changing, there is no net influence on the dominant ring total pressure and the RDI is mainly unaffected. However, for Duct-3A for -3B, the RDI is also affected by the total pressure on the inner ring, and consequently for the more central mode shapes which arise with these ducts there is more of an influence from mode 1 and the higher modes on the RDI. Nevertheless, <RDI> is still mainly dominated by mode 0. For Duct-3B, it is slightly different where mode 1 has a negligible impact, but that mode 2 plays a more notable role. This is because mode 2 for Duct-3B is the central axisymmetric mode which equates to the mode 1 for Duct-3A. The impact of modes 1 to 10 on the unsteady RDI highlights some differences between the Ducts. Duct-2 and -3B show that mode 1 has a small effect and, although particular modes are more potent than others, it is not strongly dominated by an individual and that broadly the cumulative impact of the higher modes gradually accounts for the unsteadiness in RDI. Duct-3A, however, shows that mode 1 accounts for 30% of the unsteadiness and that modes 1-4 account for about 55% of the unsteadiness. Apart from these elements, the modal reconstructions highlight that generally the unsteady distortion metrics are not strongly dominated by particular modes, but that the cumulative effects are important.

Acknowledgments

V. Conclusion

The unsteady flow field for a range of S-duct configurations has been simulated and assessed using a DDES computational method. The configurations encompass the effects of Mach number, Reynolds number and S-duct centreline offset. Analysis of the conventional distortion criteria highlights the main sensitivities to the S-duct configuration and quantifies the unsteady range of these parameters. These results illustrate the strongly dynamic nature of the flow field for both total pressure as well as swirl based distortion. For example the local swirl values are twice as large in the unsteady flow field in comparison with the time averaged flow field. Statistical analysis of the distortion metrics shows that the more aggressive duct notably reduces the DC60 distortion. However, it substantially increases the unsteady distortion of the RDI metric. Analysis of the unsteady flow field for the low offset geometry, shows signature regions of unsteadiness which are postulated to be related to the classical secondary flows as well as to the streamwise flow separation. These signatures are changed by the higher offset geometry where the unsteadiness is more broadband and the distinction between these two mechanisms is less clear. A proper orthogonal decomposition of the total pressure field at the duct exit identifies the underpinning flow modes which are associated with the overall total pressure unsteadiness distributions. For the more aggressive duct, the flow modes are notably different and highlight the reduced demarcation between the unsteady flow field mechanisms. For the low offset cases, a spectral analysis of the time-history of the POD coefficients confirms that nature of the total pressure spectral distributions and identifies the associated POD modes. An initial assessment of the relative importance of the POD modes on the unsteady aspects of the distortion provided mixed results. The most notable indication is that the mode most associated with the centreline separation for the high-offset configuration has a substantial effect on the RDI distortion metric. Overall the work indicates the levels and sensitivities of dynamic pressure and swirl based distortion for a range of S-duct configurations.

Table 7 Effect of mode 0 reconstruction on distortion metrics

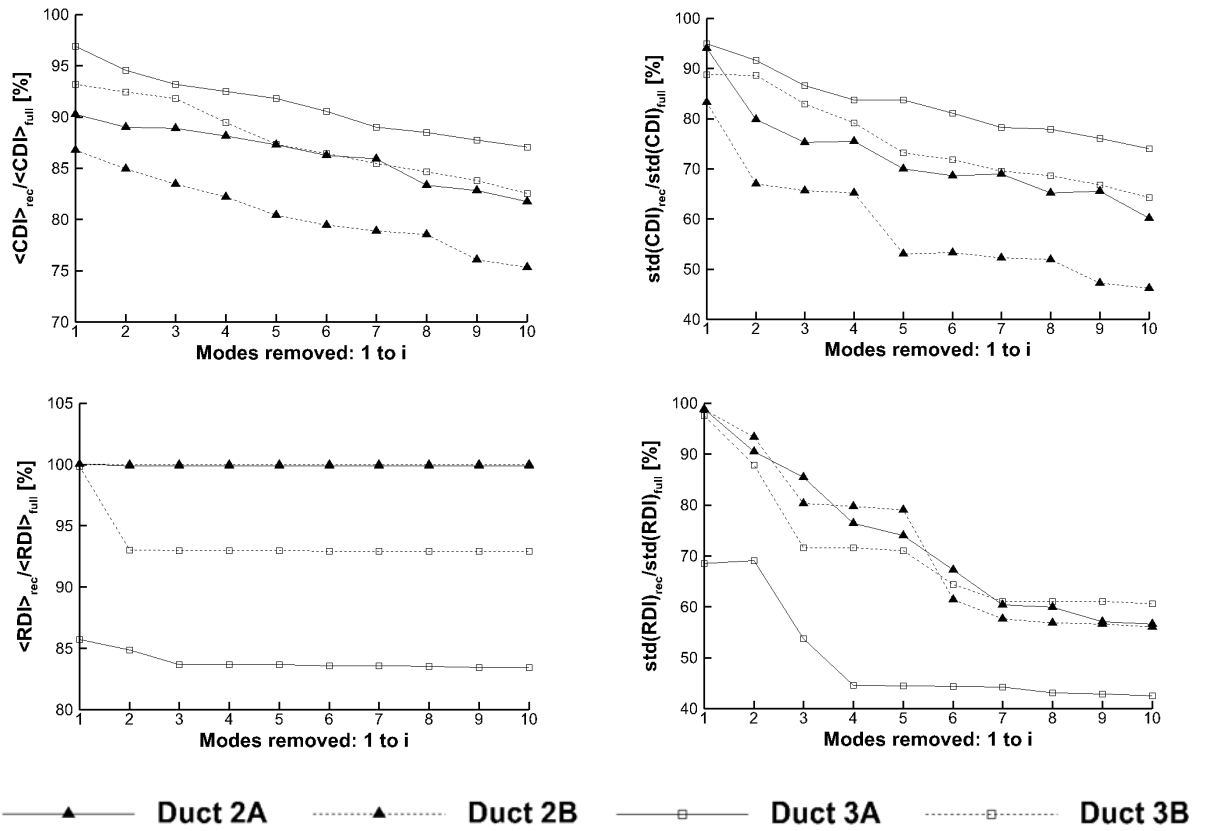| Duct 2A	All modes	Reconstruction mode 0 only	Mode 0 only %
<CDI>	0.066	0.047	71.2
<RDI>	0.033	0.032	97.0
Duct 2B			
<CDI>	0.017	0.011	64.7
<RDI>	0.009	0.009	100.0
Duct 3A			
<CDI>	0.077	0.058	75.3
<RDI>	0.036	0.030	83.3
Duct 3B			
<CDI>	0.018	0.013	72.2
<RDI>	0.009	0.008	88.9

Fig. 18 Spectral distribution of the total pressure POD coefficients.

26

References

[1] Cousins, W.T., "History, Philosophy, Physics, and Future Direction of Aircraft Propulsion System / Inlet Integration", *Proceedings of ASME Turbo Expo 2004, Power for Land, Sea, and Air*, Vienna, Austria, 2004, pp. 305-320. .

[2] S-16 Turbine Engine Inlet Flow Distortion Committee, "A Methodology for Assessing Inlet Swirl Distortion", USA: No. AIR5686, Society of Automotive Engineers, 2007.

[3] Bissinger, N. C., and Breuer, T., "Basic Principles - Gas Turbine Compatibility - Intake Aerodynamics Aspects," in Encyclopedia of Aerospace Engineering, Volume 8, Chapter EAE487, Richard Blockley and Wei Shyy, 2010.

[4] Mitchell, G. A., "Effect of Inlet Ingestion of a Wing Tip Vortex on Compressor Face Flow and Turbojet Stall Margin," Tech. Rep. TM X-3246, NASA, 1975.

[5] Mitchell, G. A., "Effect of Inlet Ingestion of a Wing Tip Vortex on Turbojet Stall Margin," NASA Tech. Rep. TM-X-71610, 1974.

[6] Meyer, W., Pazur, W., and Fottner, L., "The Influence of Intake Swirl Distortion on the Steady-State Performance of a Low Bypass Twin-Spool Engine," AGARD, Tech. Rep. CP-498, 1991.

[7] Bowditch, D. N., and Coltrin, R. E., "A Survey of Inlet/Engine Distortion Compatibility", NASA Technical Memorandum 83421, 1983

[8] Wellborn, S. R., Okiishi, T. H., and Reichert, B., "A study of the Compressible Flow Through a Diffusing S-Duct," NASA Technical Memorandum 106411, 1993.

[9] Delot, A. L., and Schamhorst, R., "A Comparison of Several CFD Codes with Experimental Data in a Diffusing S-Duct," 49th AIAA/ASME/SAE/ASEE Joint Propulsion Conference, AIAA 2013-3796, San Jose, TX, USA, 2013.

[10] Fiola, C., and Agarwal, K., "Simulation of Secondary and Separated Flow in Diffusing S Ducts", Journal of Propulsion and Power, Vol. 31, No. 1, January-February 2015, pp. 180-191.
doi: 10.2514/1.B35275

[11] Delot, A. L., Garnier, E., and Pagan, D., "Flow Control in a High-Offset Subsonic Air Intake," in 47th AIAA/ASME/SAE/ASEE Joint Propulsion Conference and Exhibit, AIAA 2011-5569, San Diego, CA, USA, 2011.
arc.aiaa.org/DOI/abs/10.2514/6.2011-5569

[12] Garnier, E., Leplat, M, Monnier, J. C., and Delva, J., "Flow control by pulsed jet in a highly bended S-duct," AIAA 2012-3250, 6th AIAA Flow Control Conference, NO , Louisiana, USA, 2012.

[13] Berens, T. M., Delot, A. L., Chevalier, M., Van Muijden, J, Waaijer, R. A., and Tattersall, P., "Numerical Simulations for High Offset Intake Diffuser Flows," AIAA 2014-0371, *AIAA 52nd Aerospace Sciences Meeting*, , National Harbor, MD, USA, 2014.

[14] Delot, A. L., Berens, T. M., Tormalm, M., Säterskog, M., and Ceresola, N., "DES Computations for a Subsonic UAS Configuration with a Highly Integrated S-Shaped Inlet Duct," AIAA 2014-0723, *AIAA 52nd Aerospace Sciences Meeting*, , MD, USA, 2014.

[15] Harloff, G.J., Reichert B.A., and Wellborn S.R., "Navier-Stokes Analysis and Experimental Data Comparison of Compressible Flow in a Diffusing S-Duct", AIAA-92-2699-CP, 1992.

[16] Spalart, P. S., "Detached-Eddy Simulation," *The Annual Review of Fluid Mechanics*, Vol. 41, 2008, pp. 181-202.
doi: 10.1146/annurev.fluid.010908.165130.

[17] Chevalier, M. and Peng, S.-H., "Detached Eddy Simulation of Turbulent Flow in a Highly Offset Intake Diffuser", *Progress in Hybrid RANS-LES Modelling*, NNFM 111, Springer-Verlag Berlin, 2010, pp. 111–121.

[18] ANSYS, "ANSYS FLUENT Theory Guide", ANSYS, Inc, Southpointe, 275 Technology Drive, Canonsburg, PA, 15317. Release 14.0. November 2011.

[19] ANSYS, "ANSYS FLUENT User Guide", ANSYS, Inc, Southpointe, 275 Technology Drive, Canonsburg, PA, 15317. Release 14.0. November 2011.

[20] Roache, P. J., "Verification and Validation in Computational Science and Engineering," Hermosa Publishers, Albuquerque, USA,, 1998.

[21] S-16 Turbine Engine Inlet Flow Distortion Committee, "Inlet Total-Pressure-Distortion Considerations for Gas-Turbine Engines," No. AIR1419, Society of Automotive Engineers, USA, 1999.

[22] Seddon, J. M., Goldsmith, E.L., *Intake Aerodynamics*, *AIAA Education Series*, 1998

[23] Cousins, W.T., "The Dynamics of Stall and Surge Behaviour in Axial-Centrifugal Compressors," Ph.D. Dissertation, Virginia Polytechnic Institute and State University, 1997.

[24] Kostas, J., Soria, J., Chong, M. S., "A Comparison Between Snapshot POD Analysis of PIV Velocity and Vorticity Data," *Experiments in Fluids*, Vol. 38, Issue 2, 2005, pp 146-160.
doi: 10.1007/s00348-004-0873-4

[25] Kostas, J., Soria, J., Chong, M. S., "Particle Image Velocimetry Measurements of a Backward-Facing Step Flow," *Experiments in Fluids,* Vol. 33, 2002, pp 838-853.
doi: 10.1007/s00348-002-0521-9

[26] Chen, H., Reuss, D. L., Hung, D., Sick, V., "A practical guide for using proper orthogonal decomposition in engine research," *International Journal of Engine Research*, Vol. 14, No. 4, 2012, pp 307-319.
doi: 10.1177/1468087412455748

[27] Gurka, R., Liberzon, A., Hetsroni, G., "POD of vorticity fields: A method for spatial characterisation of coherent structures*,", International Journal of Heat and Fluid Flow* 27, 2006, pp 416-423.

doi:10.1016/j.ijheatfluidflow.2006.01.001

[28] Vester, A. K., Orlu, R., "POD analysis of the turbulent flow downstream a mild and sharp bend*", Experiments in Fluids*, 2005, pp 56-57.

doi 10.1007/s00348-015-1926-6

[29] Holmes, P., Lumley, J. L.m Berzook, G., Rowley, C. W., *Turbulence, Coherent Structures, Dynamical Systems and Symmetry*, 2nd edition, Cambridge University Press, 2012

[30] Lumley, J. L., *Stochastic Tools in Turbulence*, Academic Press, Inc, 1970

[31] Berzook, G., Holmes, P., Lumley, J. L., "The proper orthogonal decomposition in the analysis of turbulent flows*", Annual Review of Fluid Mechanics,* Vol. 25, 1993, pp 539-75.

doi:: 10.1146/annurev.fl.25.010193.002543

[32] Sirovich, L., "Turbulence and the dynamics of coherent structures. Part 1: Coherent structures," *Quarterly of Applied Mathematics,* Vol. *XLV* , 1987, pp 561-571.